# Effect of the sun on biases in SMOS brightness temperature over ocean surfaces

**YIN Xiaobin, WANG Zhenzhan**

*Center for Space Science and Applied Research, Chinese Academy of Sciences, Beijing* 100190, *China*

**Abstract:** Up-to-date Soil Moisture and Ocean Salinity (SMOS) level 1C (L1C) Brightness Temperatures (TB), which are p rocessed with the operational prototype V5.04 and V5.05, are used to analyze the systematic biases between averaged TB measurements and simulations in Fields of View (FOV) from May 2010 to April 2012. The peak-to-peak variations in the biases are higher than 1 K in magnitude. Sun contaminations, including sun alias and sun tails, are strong sources of bias variations in the FOV. The sun correction in the level 1 (L1) image reconstruction is imperfect. By using the antenna model in L1, seasonal variations in the biases and the heating of the instrument are observed.

**Key words:** brightness temperature biases, temporal variation, ocean surface, antenna temperature, sun correction

**CLC number:** TP722.6 **Document code:** A

**Citation format:** **Yin X B and Wang Z Z. 2013. Effect of the sun on biases in SMOS brightness temperature over ocean surfaces. Journal of Remote Sensing, 17(5): 1049 – 1059 [DOI: 10.11834/jrs.20132258]**

## 1 INTRODUCTION

The SMOS mission is the European Space Agency's (ESA) second Earth Explorer Opportunity mission in its Living Planet Programme. The objective of the mission is to measure high-quality global observations of soil moisture and Sea Surface S alinity (SSS) from space (Font, et al., 2004). The SMOS satellite is equipped with an L-band microwave imaging radiometer with aperture synthesis (MIRAS) (Camps, et al., 2005; Font, et al., 2010; Yann, et al., 2010). The L band (1400 MHz to 1 427 MHz) is chosen as a tradeoff between the sufficient sensitivity of radiometric measurements to changes in ocean salinity and ground resolution constraints. The L band is a band protected for astronomy.

Since the launch of the SMOS satellite in November 2009, comparisons have been conducted between SMOS Brightness Temperatures (TBs) and forward model-simulated TBs. The s ystematic biases of several Kelvins that are dependent on locations in the Extended Alias-Free Field of View (EAFFOV) (Yin, et al., 2012a) are observed between averaged TB and simulated TB measurements. These patterns need to be removed before SSS retrievals (Tenerelli, et al., 2010). Nevertheless, imperfections in instrument calibration and image reconstructions, external noise sources (e.g., sun and galaxy), and uncertainties in the forward modeling mislead the systematic pattern estimation (Gourrion, e t al., 2012).

Therefore, we study the temporal stability of biases in the TB observed in EAFFOV from May 2010 to April 2012 by up-to-date ESA reprocessing V5.04 and V5.05.

## 2 DATA AND METHOD

### 2.1 Level 1C (L1C) TB

The MIRAS instrument onboard the SMOS satellite is a Y -shaped antenna with three arms holding 69 light cost-effective front-end receivers. This instrument measures two-dimensional images at the L-band over a range of incidence angles from 0° to 63° (with effective range from 0° to 55°) across a swath of 1 000 km with a spatial resolution of 35 km to 100 km (Fig. 1 (a)). When the satellite moves, any given area on Earth is observed more than 200 times in successive locations within the FOV (F ig. 1(b)).

In the FOV, the reconstructed linearly polarized orthogonal TB in the instrument polarization basis is denoted by TX and TY. In the absence of Faraday rotation and nominal Earth pointing, the usual horizontally polarized TB (TH) and vertically polarized TB (TV) in the surface polarization basis correspond to the r econstructed TX and TY in the instrument polarization basis a long a line through the middle of the FOV.

Real-time ESA SMOS Level 1 Operational Processor (L1OP) V5.04 and V5.05 were implemented on November 14, 2011 and the middle of March 2012, respectively. An anomaly

**Received:** 2012-09-04; **Accepted:** 2012-12-12; **Version of record first published:** 2012-12-19

**Foundation:** National Natural Science Foundation of China (No. 41076117); Scientific Research Starting Foundation for the winner of the National Excellent Doctoral Dissertations of China or Dean's award of the Chinese Academy of Sciences

**First author biography:** YIN Xiaobin (1981— ), male, Ph.D. His research interests are the passive microwave remote sensing of oceans and physical oceanography. E-mail: yinxb@yahoo.com.cn

**Corresponding author biography:** WANG Zhenzhan (1969— ), male, professor. His research interests include the microwave radiometer remote sensing of oceanic geophysical parameters, particularly in calibration/validation, retrieval algorithm development, surface emission/scattering models, and other related application study in ocean and atmospheric parameters. E-mail: wangzhenzhan@mirslab.cn

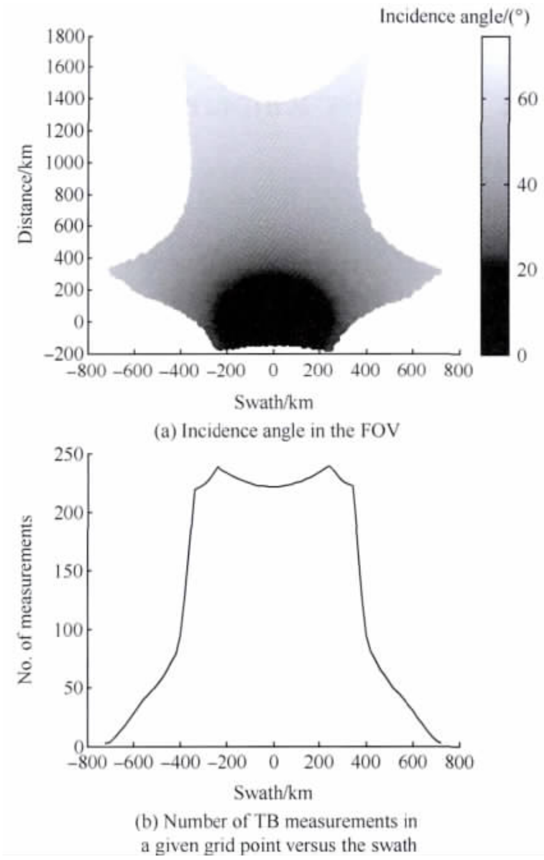


Fig. 1 Properties of MIRAS measurements

that affected the L1C sea data above 72°N and 72°S in the V 5.04 L1 processor has been fixed in V5.05. The SMOS L1C TB from January 2010 to December 2011 are reprocessed with the L1OP V5.04 and subsequently released.

We use the MIRAS TB of reprocessing (V5.04) from May 2010 to December 2011 and real-time processing (V5.04 and V 5.05) since January 2012.

## 2.2 Forward model

The forward model at the L band that computes for TB at the top of the atmosphere without considering the Faraday rotation in the Earth reference frame can be expressed as below

$$TB = ((Tb_{\mathrm{flat}} + Tb_{\mathrm{rough}})(1 - F) + Tb_{\mathrm{foam}} + Tb_{\mathrm{DN}}\Gamma + Tb_{\mathrm{gal\_ref}}) e^{-\tau_{\mathrm{atm}}} + Tb_{\mathrm{UP}} \quad (1)$$

where $Tb_{\mathrm{flat}}$ is the TB for flat sea, $Tb_{\mathrm{rough}}$ is the contribution of the roughness of the sea, $F$ is the fraction of sea foam coverage that mainly depends on Wind Speed (WS), $Tb_{\mathrm{foam}}$ is the TB of the foam, $Tb_{\mathrm{DN}}$ is the downward emitted atmospheric radiation, $\Gamma$ is the sea surface reflection coefficient, $Tb_{\mathrm{gal\_ref}}$ is the cosmic and galactic contribution scattered by the sea surface because of the directional inhomogeneities in the galactic signal, $Tb_{\mathrm{UP}}$ is the a tmospheric self-emission directed to the antenna, and $\tau_{\mathrm{atm}}$ is the atmospheric attenuation.

The forward model simulates the atmospheric emission and absorption (Liebe, et al., 1993), the scattering of celestial and a tmospheric radiation by the rough ocean surface (Reul, et al., 2008), and the emission by a rough sea surface (Yin, et al., 2012b). The sum of all simulated contributions in the sea surface polarization reference frame is computed first. A transformation matrix of the Stokes vector to the satellite antenna reference frame including the geometric and Faraday rotation (Waldteufel, et al., 2002, 2004) is applied. Therefore, simulated TBs can be compared with actual MIRAS TBs in the SMOS antenna-direction cosine frame ($\xi$, $\eta$).

The salinity used as input for the simulation is obtained from the monthly analysis of the World Ocean Atlas 2009 (A ntonov, et al., 2010). WS, Sea Surface Temperature (SST), and atmospheric parameters are obtained from forecasts provided by the European Centre for Medium-Range Weather Forecasts. The Total Electron Content (TEC) produced by the International Global Navigation Satellite System Service is used to reprocess the L1 product, whereas the TEC predicted by the International Reference Ionosphere 2000 model (Bilitza, 2001) is used for the real-time L1 product.

## 2.3 Effect of the sun

The orbit of SMOS is sun synchronous with a local equator crossing time of 06:00 am at the ascending node and an inclination of 98.3°. Hence, the sun always remains at the right-hand side of SMOS, and the alias is at the left-hand side of the E AFFOV (Camps, et al., 2004) (Fig. 2). The elevation of the sun alias in the antenna frame of the instrument depends on the season and direction of passes (ascending or descending). For a scending passes during April and August, the sun alias is located on the bottom-left of the EAFFOV. For descending passes during August and April, the sun alias is located along the alias of the unit circle on the left-hand side of the EAFFOV.

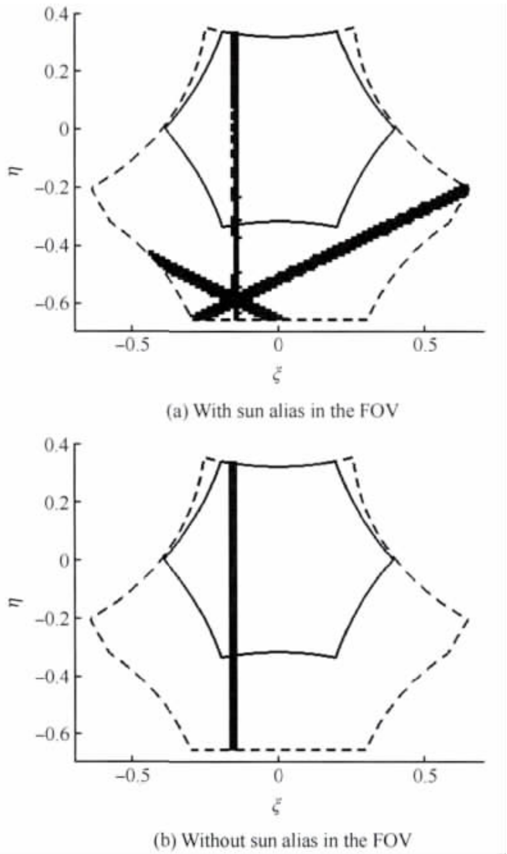


Fig. 2 Sun tails in the FOV

The direct influence of the sun can be treated as a point i nterference, which induces star-like( "* ") tails in two dimonitional FOV with the intersection of tails as the alias of the sun (Fig. 2). The sun correction method was proposed by Camps, e t al. (2004) is used in the ESA L1 V5 image reconstruction and flagging of sun alias and tails.

The scattered sun glint by the rough ocean surface is difficult to account for because of the strong temporal variations of the sun TB at the L band. The magnitudes of the scattered sun glint in different incidence angles are estimated (Reul, et al., 2007) for a ground pixel. The pixel is flagged if the estimated sun glint is stronger than 2 K for 10% of the measurements over that pixel.

The instrument heating caused by the sun also affects the reconstructed TB caused by the antenna model.

### 2.4 TB biases

The TB biases are derived by computing the differences b etween measured and modeled TB at the antenna level. Separate biases are also computed for ascending and descending passes. The SMOS L1C TB of both ascending and descending passes o ver the eastern Pacific Ocean between 45° S and 5° S are used in this study. The following diamond regions that are far from land are used: 121° ± 16° W at 5° S and 111° ± 16° W at 45° S for the ascending passes (Fig. 3(a)); 112° ± 16° W at 5° S and 123° ± 16° W at 45° S for the descending passes (Fig. 3(b)).

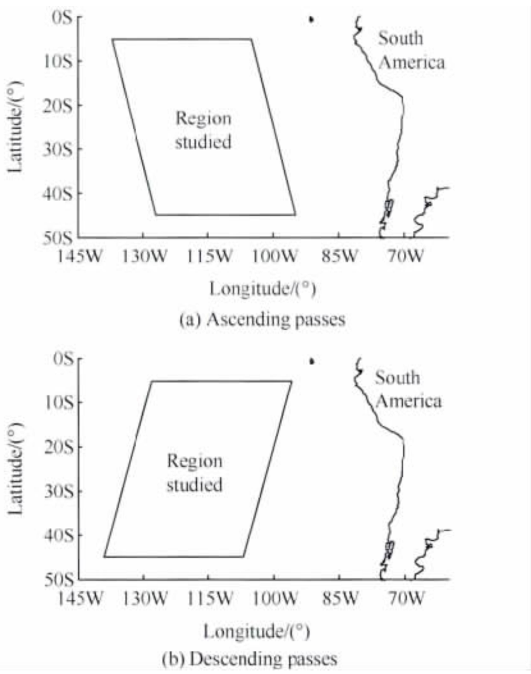


Fig. 3 Regions used

The MIRAS instrument is equipped with three Noise Injection Radiometers (NIR), which provides a precise measurement of the average TB scene for the absolute calibration of the M IRAS image and measures the noise temperature level of the internal active calibration source for each individual receiver c alibration (Colliander, et al., 2005). The NIR is present on each of the three arms of the MIRAS. The NIRs are calibrated every two weeks, and the resulting parameters are introduced in the processing.

For each NIR event, 10 ascending and 10 descending passes that fall within the diamond regions (Fig. 3) are used to compute the TB biases of the ascending and descending passes, respectively. TB biases centered on each NIR event are computed every two weeks from May 2010 to December 2011. Since January 2012, TB biases are computed once per month and are triggered by NIR events near the end or beginning of each month. A pproximately 40 and 4 sets of TB biases of ascending and d escending passes are obtained from May 2010 to December 2011 and from January 2012 to April 2012, respectively.

The nominal selection criteria of the 10 passes and MIRAS TB are provided as below:

(1) Must exceed 10000 grid points per pass that fall within the ascending (descending) South Pacific diamond region.

(2) Only grid points far from land with no ice or rain contamination must be used; ECMWF data must not be missing; passes must not be flagged as having a high TEC gradient on the dwell line; no L1C error flag set should occur; and WS must be between 3 $ms^{-1}$ and 12 $ms^{-1}$.

(3) The following measurements must be discarded: sun points, sun tails, direct sun corrections in the FOV, reflected sun corrections in the FOV, high sun glints, high galactic noises, outliers, footprint major axes exceeding 100 km, differences between specular direction and target moon direction less than 0 .5°, radio frequency interference contamination, presence of ice, and passes within 200 km from land.

More detailed information regarding the flags can be found in Section 3 of the L2OS Algorithm Theoretical Basis Document, which is available on ([2012-08-27] http://www.argans.co.uk/smos/docs/deliverables/delivered/ATBD/SO-TN-ARG-GS-0007_L2OS-ATBD_v3.8_111117.pdf).

## 3 RESULTS AND ANALYSIS

### 3.1 Variations of TB biases in the FOV

The TB biases computed on September 28, 2010 are shown in Fig. 4. In the antenna-direction cosine frame ($\xi$, $\eta$), the TB b iases in the FOV have typical amplitudes of ±10 K, and the magnitude of biases in Y polarization is higher than that in X p olarization. From May 2010 to April 2012, the peak-to-peak variations in TB biases exceed 1 K in magnitude depending on the FOV location. Diagonal stripes appear in Y polarization in the anomalies of TB biases with respect to those shown in Fig. 5. When the sun alias is in the FOV, vertical stripes are observed in the FOV because of sun contamination (Fig. 5(a)).

The effects of sun correction on TB biases are tested. Ten ascending passes computed on July 4, 2010 are reprocessed with the same L1 processor V5.04 and V5.05 without sun correction. The application of sun correction reduces the vertical stripes and sun tails in Y polarization and decreases the standard deviation of TB biases in the FOV from 0.79 K to 0.53 K. However, vertical stripes and sun tails are enhanced in X polarization even if the standard deviation of the TB biases in the FOV only exhibits slight changes (Fig. 6). The median and mean values of anomalies in the TB biases of the FOV are close (within 0.05 K) whether sun correction is applied.

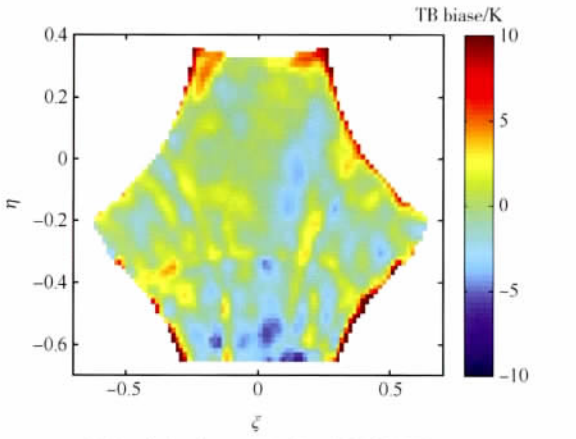

(a) X polarization,mean(std)=−0.02(2.26)/K

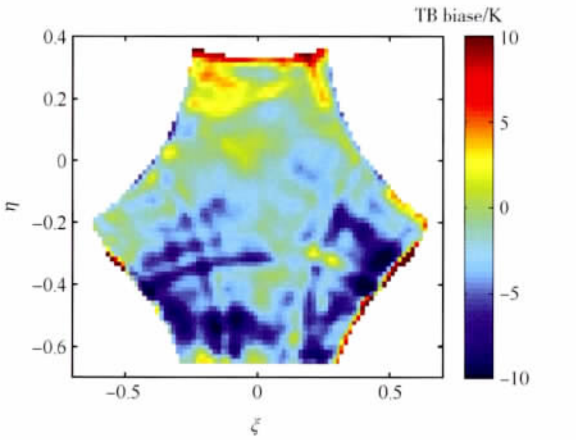

(b) Y polarization,mean(std)=−2.34(3.5)/K

Fig.4 TB biases in the FOV

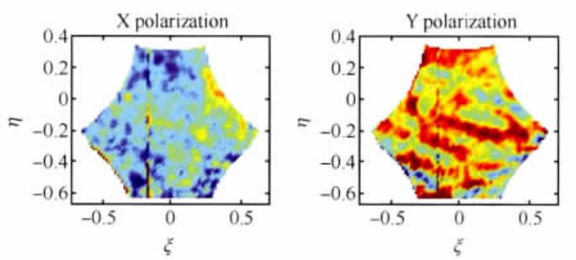

(a) Without sun alias in the FOV: X polarization median (mean)= −0.25 (−0.22) K; Y polarization median (mean) = 0.33 (0.34) K

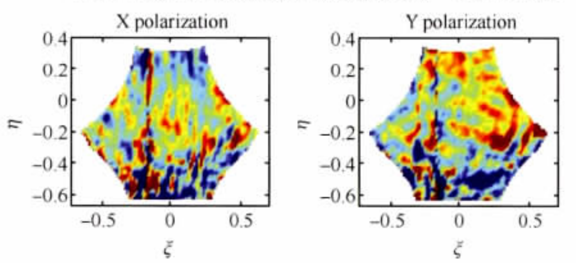

(b) With sun alias in the FOV: X polarization median (mean)= −0.03 (−0.04) K;Y polarization median (mean) = 0.07 (0.01) K

Fig.5 Anomalies in TB biases with respect to the reference shown in Fig.4

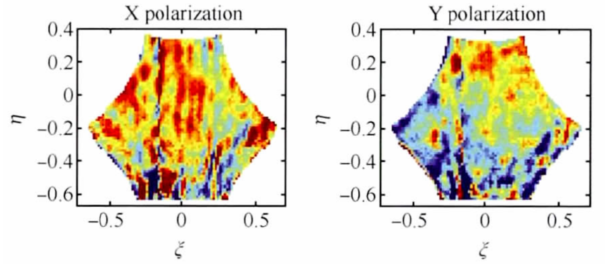

(a) Sun correction on X polarization median (standard deviation) = 0.28 (0.51) K and Y median (standard deviation) = −0.03 (0.53) K

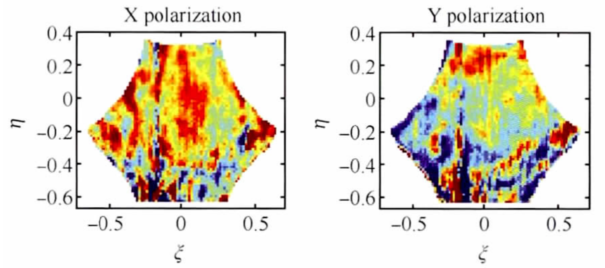


Fig. 6 Effect of sun correction on TB biases

### 3.2 Seasonal variations of TB biases

The receivers on board the MIRAS are affected by seasonal variations because of the changes in the antenna patch temperature throughout the year. Thus, a new antenna model is incorporated in ESA L1 processor V5.04 and V5.05 processing to account for these variations (Kainulainen, et al., 2012). However, seasonal variations of TB biases averaged in the FOV are still observed. Hence, we study the seasonal variations of TB biases in terms of *Stokes* 1 = (TX/2 + TY/2) to avoid the seasonal variations in TB related to the Faraday rotation. The mean *Stokes* 1 biases of descending passes and antenna patch temperature of NIRs vary in opposite phases (Fig. 7); the correlation coefficient between the two is −0.873. The correlation

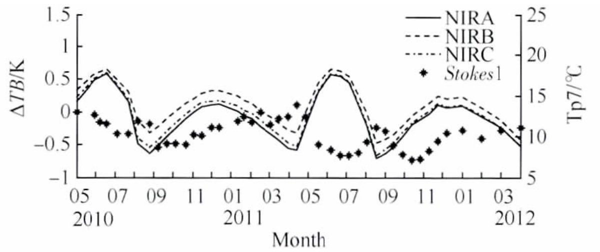

(a) Ascending passes

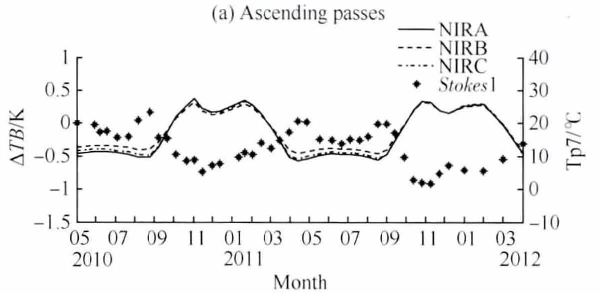

(b) Descending passes

Fig. 7 Seasonal variations of TB biases averaged in the FOV and antenna patch temperature of three NIRs (NIRA, NIRB, and NIRC) in two years between the TB biases of ascending passes and the antenna patch temperature of NIRs remains unclear. The correlation between the TB biases of ascending passes and the antenna patch temperature of NIRs is negative during months with sun alias in the FOV, whereas the correlation is positive during months without sun alias in the FOV.

In addition to seasonal evolutions, TB biases averaged along $\eta$ vary depending on the distance $\xi$ from the satellite track (Fig. 8).

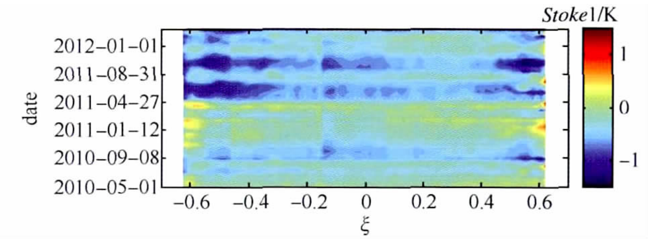


Fig. 8 Temporal evolution of TB biases averaged along dwell lines across the satellite track for two years

## 4 DISCUSSION AND CONCLUSION

TB biases in the FOV have typical amplitudes of ±10 K. For approximately two years, the peak-to-peak variations in mean Ocean Target Transformation (OTTs) are 1 K and are even larger in certain locations in the FOV.

The anomalies in the TB biases of the FOV are quite close (within 0.05 K) whether sun correction is applied. Therefore, the seasonal variations in TB biases averaged in the FOV are not caused by sun correction in the L1 image reconstruction, although the sun correction algorithm and the flag implemented in L1 V5 remain imperfect.

The seasonal variation of the TB biases of descending passes in terms of *Stokes* 1 is negatively correlated with the a ntenna patch temperature of NIRs. The correlation between the TB biases of ascending passes and antenna patch temperature of NIRs is negative during months when the sun alias is in the FOV. However, the correlation during months without sun alias in the EAF-FOV is less clear and sometimes positive. The sun i nfluences the back lobes of the instrument during the period when the instrument is at the back of the platform.

## REFERENCES


Antonov J I, Seidov D, Boyer T P, Locarnini R A, Mishonov A V, Garcia H E, Baranova O K, Zweng M M and Johnson D R. 2010. World Ocean Atlas 2009, Volume 2: Salinity. S. Levitus, Ed. NOAA Atlas NESDIS 69, U. S. Government Printing Office, Washington, D. C., 184 pp.

Bilitza D. 2001. International Reference Ionosphere 2000. Radio Science, 36(2): 261 - 275 [DOI: 10.1029/2000RS002432]

Camps A, Vall-llossera M, Duffo N, Torres F and Corbella I. 2005. Performance of sea surface salinity and soil moisture retrieval algorithms with different auxiliary datasets in 2-D L-Band aperture synthesis interferometric radiometers. IEEE Transactions on Geoscience and Remote Sensing, 43(5): 1189 - 1200 [DOI: 10.1109/TGRS.2004.842096]

Camps A, Vall-llossera M, Duffo N, Zapata M, Corbella I, Torres F and Barrena V. 2004. Sun effects in 2-D aperture synthesis radiometry imaging and their cancelation. IEEE Transactions on Geoscience and Remote Sensing, 42(6): 1161 - 1167 [DOI: 10.1109/TGRS.2004.826561]

Colliander A, Tauriainen S, Auer T I, Kainulainen J, Uusitalo J, Toikka M and Hallikainen M T. 2005. MIRAS reference radiometer: a fully polarimetric noise injection radiometer. IEEE Transactions on Geoscience and Remote Sensing, 43(5): 1135 - 1143 [DOI: 10.1109/TGRS.2004.840667]

Font J, Camps A, Borges A, Martín-Neira M, Boutin J, Reul N, Kerr Y, Hahne A and Mecklenburg S. 2010. SMOS: The challenging sea surface salinity measurement from space. Proceedings of the IEEE, 98(5): 649 - 665 [DOI: 10.1109/JPROC.2009.2033096]

Font J, Lagerloef G S E, Le Vine D M, Camps A and Zanifé O Z. 2004. The determination of surface salinity with the European SMOS space mission. IEEE Transactions on Geoscience and Remote Sensing, 42(10): 2196 - 2205 [DOI: 10.1109/TGRS.2004.834649]

Gourrion J, Sabia R, Portabella M, Tenerelli J, Guimbard S and Camps A. 2012. Characterization of the SMOS instrumental error pattern correction over the Ocean. IEEE Geoscience and Remote Sensing Letters, 9(4): 793 - 797 [DOI: 10.1109/LGRS.2011.2181990]

Kainulainen J, Colliander A, Closa J, Martin-Neira M, Oliva R, Buenadicha G, Alcaine P, Hakkarainen A and Hallikainen M T. 2012. Radiometric performance of the SMOS reference radiometers—Assessment after one year of operation. IEEE Transactions on Geoscience and Remote Sensing, 50(5): 1367 - 1383 [DOI: 10.1109/TGRS.2011.2177273]

Kerr Y H, Waldteufel P, Wigneron J P, Delwart S, Cabot F, Boutin J, Escorihuela M J, Font J, Reul N, Gruhier C, Juglea S E, Drinkwater M R, Hahne A, Martin-Neira M and Mecklenburg S. 2010. The SMOS mission: new tool for monitoring key elements of the global water cycle. Proceedings of the IEEE, 98(5): 666 - 687 [DOI: 10.1109/JPROC.2010.2043032]

Liebe H, Hufford G and Cotton M. 1993. Propagation modeling of moist air and suspended water/ice particles at frequencies below 1000 Ghz // Proceedings of NATO/AGARD Wave Propagation Panel, 52nd meeting, Mallorca, Spain, 3: 1 - 10

Mecklenburg S, Drusch M, Kerr Y H, Font J, Martin-Neira M, Delwart S, Buenadicha G, Reul N, Daganzo-Eusebio E, Oliva R and Crapolicchio R 2012 ESA's soil moisture and ocean salinity mission: Mission performance and operations. IEEE Transactions on Geoscience and Remote Sensing, 50(5): 1354 - 1366 [DOI: 10.1109/TGRS.2012.2187666]

Reul N, Tenerelli J E, Chapron B and Waldteufel P. 2007. Modeling sun glitter at L-band for sea surface salinity remote sensing with SMOS. IEEE Transactions on Geoscience and Remote Sensing, 45(7): 2073 - 2087 [DOI: 10.1109/TGRS.2006.890421]

Reul N, Tenerelli J E, Floury N and Chapron B. 2008. Earth-viewing L-band radiometer sensing of sea surface scattered celestial sky radiation. Part II: Application to SMOS. IEEE Transactions on Geoscience and Remote Sensing, 46(3): 675 - 688 [DOI: 10.1109/TGRS.2007.914804]

Tenerelli J and Reul N. 2010. SMOS brightness temperatures over the global oceans: Contaminating effects and salinity retrieval // Proceedings of the ESA Living Planet Symposium, Bergen, Norway, 2010, ESA SP-686

Waldteufel P and Caudal G. 2002. About off-axis radiometric polarimetric measurements. IEEE Transactions on Geoscience and Remote Sensing, 40(6): 1435 - 1439 [DOI: 10.1109/TGRS.2002.800236]

Waldteufel P, Floury N, Dinnat E P and Caudal G. 2004. Ionospheric effects for L-band 2-D interferometric radiometry. IEEE Transactions on Geoscience and Remote Sensing, 42(1): 105 - 118 [DOI: 10.1109/TGRS.2003.817685]

Yin X B, Boutin J and Spurgeon P. 2012a. First assessment of SMOS data over open ocean: Part I-Pacific Ocean. IEEE Transactions on Geoscience and Remote Sensing, 50(5): 1648 - 1661 [DOI: 10.1109/TGRS.2012.2188407]

Yin X B, Boutin J, Martin N and Spurgeon P. 2012b. Optimization of L-Band sea surface emissivity models deduced from SMOS data. IEEE Transactions on Geoscience and Remote Sensing, 50(5): 1414-1426 [DOI: 10.1109/TGRS.2012.2184547]

# 太阳对SMOS卫星海表亮温偏差年际变化的影响

殷晓斌，王振占

中国科学院 空间科学与应用研究中心，北京 100190

摘 要：利用欧洲空间局发布的土壤湿度和盐度卫星最新版本V5.04及V5.05的2010年5月至2012年4月的L1C级亮温数据，分析了其2维视场中存在的亮温偏差和年际变化。亮温偏差在视场中的分布不均匀并随季节变化。其年际变化超过1 K。太阳及其尾迹在视场中的位置随季节变化并对该卫星测量的亮温产生影响，是亮温偏差年际变化的主要来源。另外，太阳高度角的季节性变化会使该卫星天线的物理温度产生季节性变化，并通过天线模型使其测量亮温产生季节性偏差。

关键词：亮温偏差，季节变化，海表面，天线温度，太阳修正

中图分类号：TP722.6　　文献标志码：A

引用格式：殷晓斌，王振占.2013.太阳对SMOS卫星海表亮温偏差年际变化的影响.遥感学报，17(5)：1049－1059

Yin X B and Wang Z Z. 2013. Effect of the sun on biases in SMOS brightness temperature over ocean surfaces. Journal of Remote Sensing，17(5)：1049－1059 [DOI：10.11834/jrs.20132258]

## 1 引 言

欧洲空间局土壤湿度和盐度卫星(SMOS卫星)计划，是其"Living Planet"计划的第2个"Earth Explorer Opportunity"项目。该项目的目标是提供高质量的土壤湿度和海表面盐度(SSS)的全球卫星观测数据(Font 等，2004)。SMOS卫星的唯一载荷Microwave Imaging Radiometer using Aperture Synthesis(MIRAS)是全球第1个在轨L波段综合孔径辐射计(Camps 等，2005；Font 等，2010；Kerr 等，2010)。L波段(1400—1427 MHz)是亮温对SSS变化的灵敏度和天线地面分辨率的折中选择，同时也是天文观测保护频段。

自从2009年11月SMOS卫星发射以来，人们利用亮温模型对该卫星测量的亮温进行了大量的比对和验证工作。研究表明，SMOS卫星测量的亮温存在一个系统偏差，该偏差与视场中的位置有关(Yin 等，2012a)。欧洲空间局反演软件进行盐度反演前，需要将该偏差移除(Tenerelli 和 Reul，2010)。设备定标方法和图像重构方法不完善、外部干扰源(太阳、银河等)以及亮温模型的不准确性，对人们给估视场中的亮温偏差带来一定的困难(Gourrion 等，2012)。

本文利用欧洲空间局发布的最新版本V5.04和V5.05的L1级亮温数据，分析了2010年5月至2012年4月的两年间该卫星2维视场中存在的亮温偏差和年际变化。

## 2 数据和方法

### 2.1 L1C亮温

MIRAS综合孔径辐射计的Y型阵列共载有69个接收机和其他若干辅助设备。该辐射计一次性生成地表亮温辐射的2维图像，观测入射角范围为0°—63°(有效范围0°—55°)，刈幅宽度超过1 000 km(图1(a))，有效地面分辨率为35—100 km。卫星单次过境时，地表同一面元可以被不同入射角测量最多超过200次(图1(b))。

地球坐标系下水平(垂直极化)亮温TH(TV)经旋转为天线坐标系下的亮温TX和TY。当法拉第旋转效应为0时，视场正中直线上的亮温TX与TH相等，亮温TY与TV相等。

收稿日期：2012-09-04；修订日期：2012-12-12；优先数字出版日期：2012-12-19

基金项目：国家自然科学基金(编号：41076117)；中国科学院"优秀博士学位论文、院长奖获得者科研启动经费专项基金"

第一作者简介：殷晓斌(1981— )，男，博士，现从事海洋微波辐射遥感机理和物理海洋应用研究。E-mail：yinxb@yahoo.com.cn

通信作者简介：王振占(1969— )，男，研究员，主要从事微波遥感新技术及应用技术研究。E-mail：wangzhenzhan@mirslab.cn

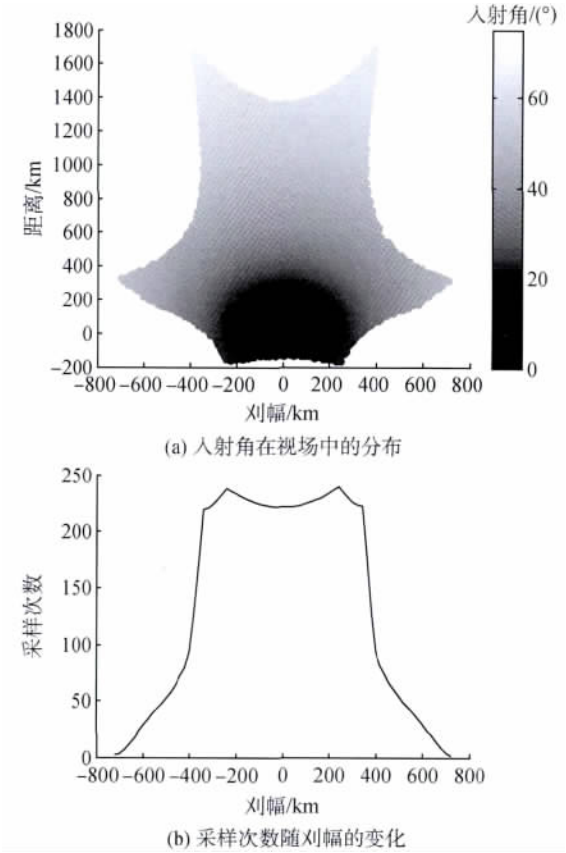

(a) 入射角在视场中的分布

(b) 采样次数随刈幅的变化

图 1　MIRAS 测量参数

V5.04 版本的 L1 级处理器自 2011 年 11 月 14 日开始业务化运行，最新版本的 V5.05 处理器自 2012 年 3 月中旬开始运行。V5.05 版本修正了 V 5.04版本在 72°以上高纬地区海洋格点处理异常的错误。同时，欧洲空间局使用 V5.04 版本的 L1 级处理器对 SMOS 卫星 2010 年 1 月至 2011 年 12 月的数据进行了重新处理。

本文使用 2010 年 5 月至 2011 年 12 月的 L1 V5.04 版本的重新处理 L1C 亮温数据以及 2012 年的 V5.04 及 V5.05 版本的 L1C 亮温实时处理数据进行研究。

## 2.2　亮温模拟

L 波段微波辐射传输模型为

$$TB = ((Tb_{\mathrm{flat}} + Tb_{\mathrm{rough}})(1 - F) + Tb_{\mathrm{foam}} + Tb_{\mathrm{DN}} \cdot \Gamma + Tb_{\mathrm{gal\_ref}}) e^{-\tau_{\mathrm{atm}}} + Tb_{\mathrm{UP}} \quad (1)$$

式中，$Tb_{\mathrm{flat}}$是平静海面亮温辐射，$Tb_{\mathrm{rough}}$是海表面粗糙度的亮温贡献，$F$ 是海表泡沫覆盖率，$Tb_{\mathrm{foam}}$是泡沫的亮温辐射，$Tb_{\mathrm{DN}}$是大气下行辐射，$\Gamma$ 是海表反射系数，$Tb_{\mathrm{gal_ref}}$是经海表散射的宇宙背景辐射，$Tb_{\mathrm{UP}}$是大气上行辐射，$\tau_{\mathrm{atm}}$是大气衰减系数。

本文采用 Liebe 等人(1993)的算法计算大气亮温辐射和衰减系数，Reul 等人(2008)的算法计算 $Tb_{\mathrm{gal\_ref}}$，Yin 等人(2012b)的模型计算海表面粗糙度和泡沫的亮温贡献。式(1)的亮温需要进行几何和法拉第旋转(Waldteufel 等，2004；Waldteufel 和 Caudal，2002)以便和 MIRAS 亮温在方向余弦天线坐标系($\xi$，$\eta$)下进行对比。

亮温模型的盐度输入取自 World Ocean Atlas 2009(Antonov 等，2010)，风场、海表面温度和大气参数为 European Centre for Medium-Range Weather Forecasts 预报值。大气总电子含量 TEC (Total Electron Content)再分析 L1 重处理器重新处理数据，L1 处理器实时处理的数据采用 International Reference Ionosphere 2000 (Bilitza，2001)模型值。以上数据均由欧洲空间局数据中心提供并与 MIRAS L1C 亮温数据进行匹配。

## 2.3　太阳对 MIRAS 亮温的影响

SMOS 采用太阳同步轨道 98.3°，轨道倾角升轨在当地时间 06:00 am 通过赤道。太阳一年四季均在其右方。由于 2 维综合孔径辐射计傅里叶图像合成的混叠效应，太阳的像(alias)和海面反射的太阳的像会出现在视场左侧(Camps 等，2004)(图 2)，对 MIRAS 测量的海表亮温产生影响。太阳的像在升降轨视场中的位置不同，而且位置随季节变化。对于升轨，太阳的像每年 4 月到 8 月期间出现在视场的左下角，其他时间不会出现在视场中；对于降轨，太阳的像在每年 8 月到次年 4 月期间会出现在视场中，并且随季节在很大的范围内移动。

可以将太阳的直接影响近似为点源干扰，其干扰会在 MIRAS 的 2 维视场中产生“* ”星型干扰尾迹，尾迹的交点即为太阳的像(图 2)。

V5.04 及 V5.05 版本的 L1 级数据处理器的图像重构算法使用 Camps 等人(2004)方法消除太阳的直接影响，并标识太阳的像和太阳尾迹在视场中的位置。

MIRAS 2 维视场中影响粗糙海面反射太阳耀斑的因素较多，计算比较困难，无法有效修正。目前，欧洲空间局 SMOS L2 级数据处理器采用 Reul 等人(2007)的方法估算 MIRAS 测量的地表面元不同入射角对应的海面反射太阳耀斑。当该面元超过 10% 的测量采样对应的海面反射太阳耀斑大于 2 K，即将该面元标识为受海面反射太阳耀斑强烈干扰并舍弃。

另外，太阳对天线的加热效应也会通过天线模

型影响 L1C 亮温。

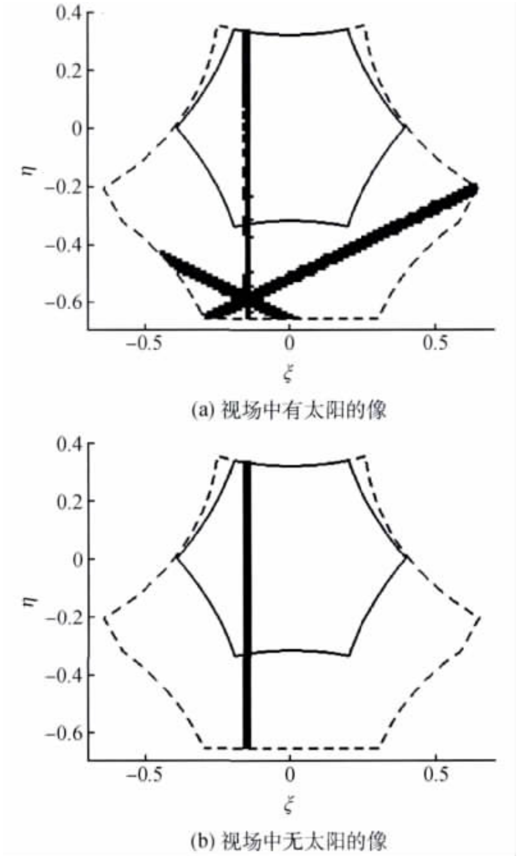


图 2 太阳尾迹示意图

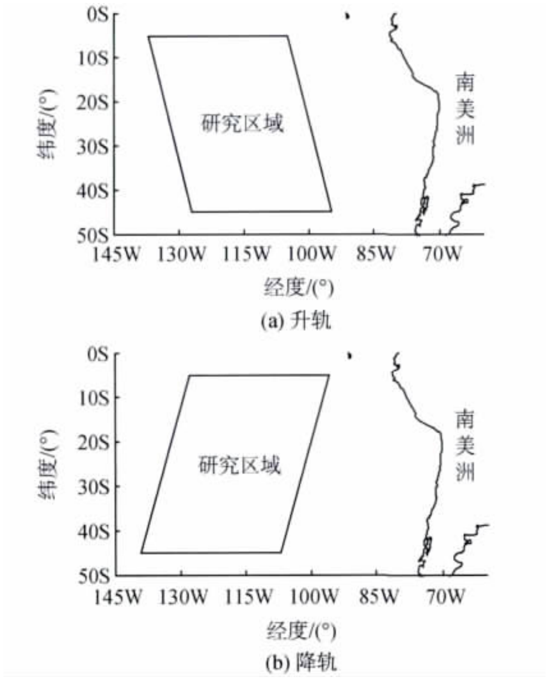


图 3 研究区域

### 2.4 亮温偏差计算

本文选取东太平洋远离陆地和岛屿的海区作为研究区域计算亮温偏差。为升轨选取的区域为 121 ±16W @ 5S,111 ±16W @ 45S (图 3(a));为降轨选取的区域为 112 ±16W @ 5S,123 ±16W @ 45S (图 3(b))。

噪声注入辐射计 NIR (Noise Injection Radiometer) 是 MIRAS 的主要功能单元之一。它可以提供 MIRAS 图像定标所需的精确平均亮温,还可以测量用于单个接收机定标的内定标源的噪声水平(Colliander 等,2005)。MIRAS 3 个臂展上各有 1 个 NIR。NIR 大约每两周定标一次(Mecklenburg 等,2012)。自 2010 年 5 月至 2011 年 12 月,针对每次 NIR 定标,选取经过图 3 所示区域的 10 个升轨或者 10 个降轨分别计算升轨和降轨的平均亮温偏差。自 2012 年 1 月起,每月计算一次平均亮温偏差。计算这些亮温偏差所选取的轨道和频率与欧洲空间局的 V5.50 L2 级数据处理器 V5.5 海表面盐度反演时修正用的亮温偏差完全一致。2010 年 5 月—2011 年 12 月,总计有 40 个亮温偏差序列;2012 年 1 月—4 月有 4 个序列。

MIRAS 亮温数据筛选标准如下:

(1) 在东太平洋所选研究海区,单轨有效测量海面面元超过 10000 个;

(2) 面元 200 km 内无岛屿,无降水,无强 TEC 梯度,10 m 高处等效风速范围 3—12 $ms^{-1}$;

(3) 无太阳以及太阳尾迹的像影响,无强海面反射太阳耀斑影响,无月球的像影响,无强海面散射宇宙背景辐射影响,无射频干扰(Radio Frequency Interferences)影响。

欧洲空间局 L2 盐度算法文档给出了详细的数据筛选方法([2012-08-27] http://www.argans.co.uk/smos/docs/deliverables/delivered/ATBD/SO-TN-ARG-GS-0007_L2OS-ATBD_v3.8_111117.pdf)。

## 3 数据结果与分析

### 3.1 亮温偏差在视场中的变化

图 4 给出了 2010 年 9 月 28 日 10 个升轨的平均亮温偏差。结果表明,方向余弦天线坐标系($\xi$, $\eta$)下视场中的亮温偏差为 ±10 K,Y 极化亮温偏差比 X 极化大。2010 年 5 月—2012 年 4 月,亮温偏差的变化范围超过 1 K。亮温偏差随季节变化明显。无论太阳的像是否出现在视场中,Y 极化的亮温偏差变化呈现条带状斜纹(图 5)。太阳的像出现在视场中的季节,在视场中将出现竖条状纹路(图 5(a))。

这是由太阳的强干扰造成的。

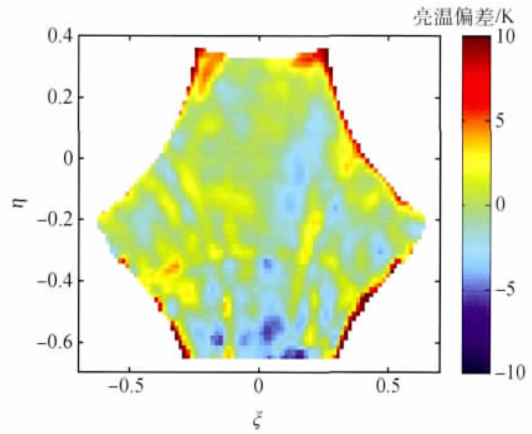


(a) X极化,均值(均方差)=-0.02(2.26)/K

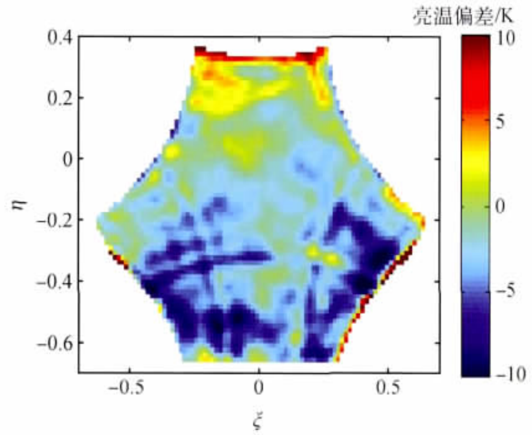


(b) Y极化,均值(均方差)=-2.34(3.5)/K

图 4 视场中的亮温偏差

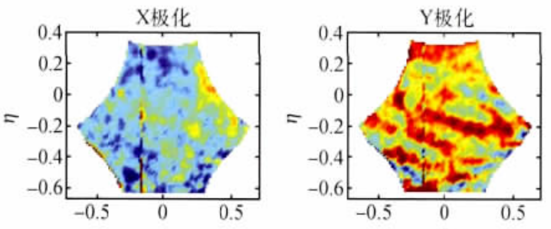


(a) 视场中无太阳的像,X极化中值(均值)为-0.25(-0.22) K,
Y极化中值(均值)为0.33(0.34) K

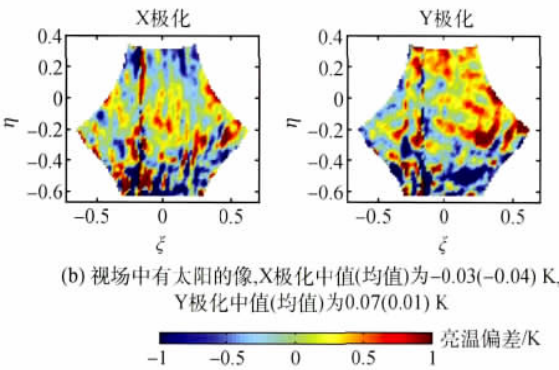


(b) 视场中有太阳的像,X极化中值(均值)为-0.03(-0.04) K,
Y极化中值(均值)为0.07(0.01) K

图 5 相对于图 3 中亮温偏差的差异示意图

本文还测试了太阳修正算法对视场中亮温偏差的影响。本文重新处理了 2010 年 7 月 4 日左右 10 个升轨的 L1C 亮温,处理时没有进行太阳修正,其他处理方法与欧洲空间局所采用方法完全一致。图 6 表明,当采用太阳修正时,Y 极化视场中的垂直条纹在很大程度上被消除了,视场中亮温偏差的均方差由 0.79 K 降低为 0.53 K; X 极化视场中的垂直条纹却增强了,而且视场中亮温偏差的均方差相对于无太阳修正的情况并无太大的变化。无论是否采用太阳修正算法,视场中的亮温偏差均值和中值变化很小。本文测试了一些其他的轨道,采用太阳修正与否,视场中的亮温偏差差异小于 0.05 K。目前所采用的太阳修正算法在定位太阳位置以及插值算法方面存在问题,仍需要改进。

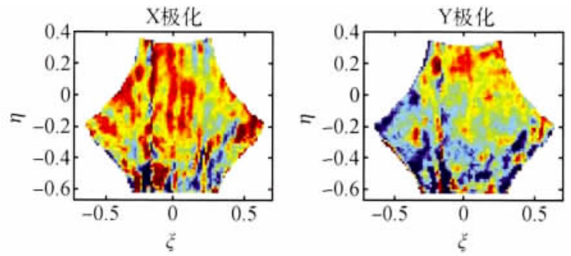


(a) 应用太阳修正,X极化中值(均方差)为0.28(0.51) K,
Y极化中值(均方差)为-0.03(0.53) K

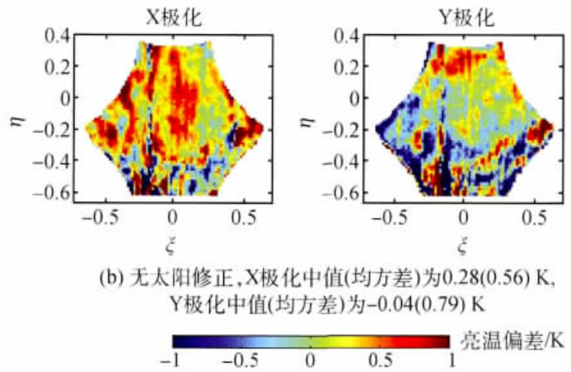


(b) 无太阳修正,X极化中值(均方差)为0.28(0.56) K,
Y极化中值(均方差)为-0.04(0.79) K

**图 6 太阳修正对亮温偏差的影响**

## 3.2 视场中平均亮温偏差的季节变化

MIRAS 的天线物理温度存在较强的季节变化,这直接影响了接收机的工作。L1 数据处理器采用了新的天线模型以修正天线物理温度变化对接收机的影响(Kainulainen 等, 2012)。但是,视场中平均亮温偏差仍存在季节变化。图 7 给出了视场中第一斯托克斯参数 $Stokes\ 1 = (TX/2 + TY/2)$ 的平均偏差和 3 个噪声注入辐射计(NIRA, NIRB 和 NIRC)物理温度随时间的变化。对于降轨,视场中 *Stokes* 1 的平均偏差的变化与 NIR 物理温度在相位一致,幅度上呈现强负相关性,二者相关系数为 -0.873。对于

升轨,视场中 *Stokes* 1 的平均偏差的变化随 NIR 物理温度的变化比较复杂: 在太阳的像出现在视场中的季节 4 月—8 月期间,*Stokes* 1 的平均偏差的变化与 NIR 物理温度变化趋势相反; 而在太阳的像不出现在视场中的季节 9 月—次 3 月期间,二者变化趋势相同,这个季节太阳出现在天线的背面。

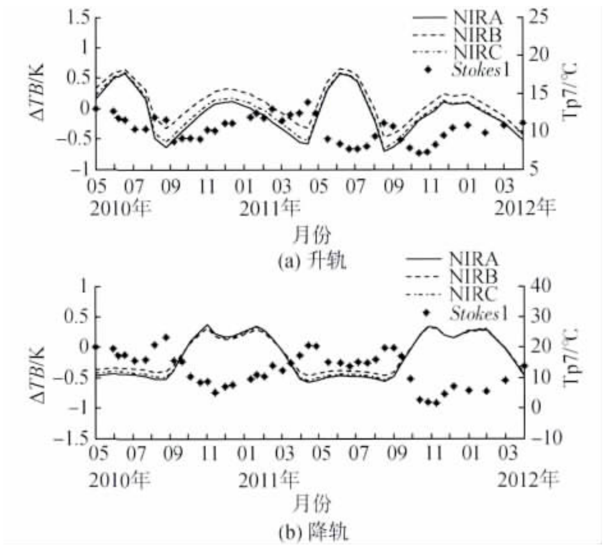


图 7 视场中第一斯托克斯参数 *Stokes* 1 的平均偏差 $\Delta TB$ 和 3 个噪声注入辐射计(NIRA, NIRB 和 NIRC)物理温度随时间的变化

*Stokes* 1 不受法拉第旋转的影响,因此图 6 中的 *Stokes* 1 季节变化与法拉第旋转效应的季节变化无关。图 8 给出了视场中距离 $\eta$ 方向平均的亮温偏差随方向余弦天线坐标系下刈幅 $\xi$ 和时间的变化。亮温偏差在刈幅方向的变化也不均匀。

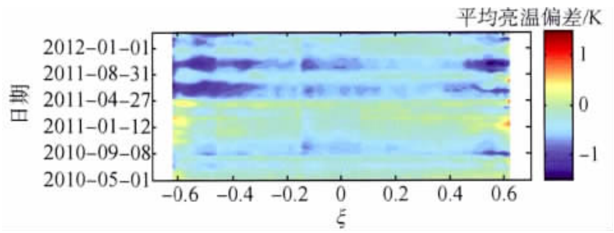


图 8 视场中距离 $\eta$ 方向平均亮温偏差随刈幅($\xi$)和时间的变化

## 4 结 论

MIRAS 视场中的亮温偏差为 ±10 K,该偏差在视场中的分布不均匀。视场中不同位置处的亮温偏差随季节变化不同。2010 年 5 月至 2012 年 4 的两年间,该偏差变化超过 1 K。太阳在 MIRAS 视场中的位置随季节变化并通过太阳和太阳尾迹的干扰影响了视场中亮温偏差的季节性变化。

此外还将视场中的亮温偏差进行了平均,并研究了该平均亮温偏差的季节性变化。3.1 小节,已经测试过,采用太阳修正与否,视场中的亮温偏差差异小于 0.05 K。因此太阳对亮温图像的直接干扰并不是视场中平均亮温偏差的季节变化的主要影响因素。目前欧洲空间局图像处理算法所采用的太阳修正算法在定位太阳位置以及插值算法方面存在问题,无法有效消除太阳对亮温图像的影响,仍需要改进。

视场中的平均亮温偏差的季节性变化主要与天线物理温度季节变化有关。太阳高度角的季节性变化会使该卫星天线的物理温度产生季节性变化,并通过天线模型影响该卫星测量亮温。对于降轨,视场中 *Stokes* 1 的平均偏差的变化与天线物理温度在相位和幅度上均呈现强负相关性。对于升轨,视场中 *Stokes* 1 的平均偏差的变化随 NIR 物理温度的变化比较复杂,太阳出现在天线背面时,对天线的背瓣可能有明显的影响。欧洲空间局目前所采用的新的天线模型仍未解决天线物理温度季节变化对测量亮温的影响。

## 参考文献(References)

Antonov J I, Seidov D, Boyer T P, Locarnini R A, Mishonov A V, Garcia H E, Baranova O K, Zweng M M and Johnson D R. 2010. World Ocean Atlas 2009, Volume 2: Salinity. S. Levitus, Ed. NOAA Atlas NESDIS 69, U. S. Government Printing Office, Washington, D. C., 184 pp.

Bilitza D. 2001. International Reference Ionosphere 2000. Radio Science, 36(2): 261 – 275 [DOI: 10.1029/2000RS002432]

Camps A, Vall-llossera M, Duffo N, Torres F and Corbella I. 2005. Performance of sea surface salinity and soil moisture retrieval algorithms with different auxiliary datasets in 2-D L-Band aperture synthesis interferometric radiometers. IEEE Transactions on Geoscience and Remote Sensing, 43(5): 1189 – 1200 [DOI: 10.1109/TGRS.2004.842096]

Camps A, Vall-llossera M, Duffo N, Zapata M, Corbella I, Torres F and Barrena V. 2004. Sun effects in 2-D aperture synthesis radiometry imaging and their cancelation. IEEE Transactions on Geoscience and Remote Sensing, 42(6): 1161 – 1167 [DOI: 10.1109/TGRS.2004.826561]

Colliander A, Tauriainen S, Auer T I, Kainulainen J, Uusitalo J, Toikka M and Hallikainen M T. 2005. MIRAS reference radiometer: a fully polarimetric noise injection radiometer. IEEE Transactions on Geoscience and Remote Sensing, 43(5): 1135 – 1143 [DOI: 10.1109/TGRS.2004.840667]

Font J, Camps A, Borges A, Martín-Neira M, Boutin J, Reul N, Kerr Y, Hahne A and Mecklenburg S. 2010. SMOS: The challenging sea surface salinity measurement from space. Proceedings of the IEEE, 98(5): 649-665 [DOI: 10.1109/JPROC.2009.2033096]

Font J, Lagerloef G S E, Le Vine D M, Camps A and Zanifé O Z. 2004. The determination of surface salinity with the European SMOS space mission. IEEE Transactions on Geoscience and Remote Sensing, 42(10): 2196-2205 [DOI: 10.1109/TGRS.2004.834649]

Gourrion J, Sabia R, Portabella M, Tenerelli J, Guimbard S and Camps A. 2012. Characterization of the SMOS instrumental error pattern correction over the Ocean. IEEE Geoscience and Remote Sensing Letters, 9(4): 793-797 [DOI: 10.1109/LGRS.2011.2181990]

Kainulainen J, Colliander A, Closa J, Martin-Neira M, Oliva R, Buenadicha G, Alcaine P, Hakkarainen A and Hallikainen M T. 2012. Radiometric performance of the SMOS reference radiometers—Assessment after one year of operation. IEEE Transactions on Geoscience and Remote Sensing, 50(5): 1367-1383 [DOI: 10.1109/TGRS.2011.2177273]

Kerr Y H, Waldteufel P, Wigneron J P, Delwart S, Cabot F, Boutin J, Escorihuela M J, Font J, Reul N, Gruhier C, Juglea S E, Drinkwater M R, Hahne A, Martin-Neira M and Mecklenburg S. 2010. The SMOS mission: new tool for monitoring key elements of the global water cycle. Proceedings of the IEEE, 98(5): 666-687 [DOI: 10.1109/JPROC.2010.2043032]

Liebe H, Hufford G and Cotton M. 1993. Propagation modeling of moist air and suspended water/ice particles at frequencies below 1000 Ghz // Proceedings of NATO/AGARD Wave Propagation Panel, 52nd meeting, Mallorca, Spain, 3: 1-10

Mecklenburg S, Drusch M, Kerr Y H, Font J, Martin-Neira M, Delwart S, Buenadicha G, Reul N, Daganzo-Eusebio E, Oliva R and Crapolicchio R 2012 ESA's soil moisture and ocean salinity mission: Mission performance and operations. IEEE Transactions on Geoscience and Remote Sensing, 50(5): 1354-1366 [DOI: 10.1109/TGRS.2012.2187666]

Reul N, Tenerelli J E, Chapron B and Waldteufel P. 2007. Modeling sun glitter at L-band for sea surface salinity remote sensing with SMOS. IEEE Transactions on Geoscience and Remote Sensing, 45(7): 2073-2087 [DOI: 10.1109/TGRS.2006.890421]

Reul N, Tenerelli J E, Floury N and Chapron B. 2008. Earth-viewing L-band radiometer sensing of sea surface scattered celestial sky radiation. Part II: Application to SMOS. IEEE Transactions on Geoscience and Remote Sensing, 46(3): 675-688 [DOI: 10.1109/TGRS.2007.914804]

Tenerelli J and Reul N. 2010. SMOS brightness temperatures over the global oceans: Contaminating effects and salinity retrieval // Proceedings of the ESA Living Planet Symposium, Bergen, Norway, 2010, ESA SP-686

Waldteufel P and Caudal G. 2002. About off-axis radiometric polarimetric measurements. IEEE Transactions on Geoscience and Remote Sensing, 40(6): 1435-1439 [DOI: 10.1109/TGRS.2002.800236]

Waldteufel P, Floury N, Dinnat E P and Caudal G. 2004. Ionospheric effects for L-band 2-D interferometric radiometry. IEEE Transactions on Geoscience and Remote Sensing, 42(1): 105-118 [DOI: 10.1109/TGRS.2003.817685]

Yin X B, Boutin J and Spurgeon P. 2012a. First assessment of SMOS data over open ocean: Part I-Pacific Ocean. IEEE Transactions on Geoscience and Remote Sensing, 50(5): 1648-1661 [DOI: 10.1109/TGRS.2012.2188407]

Yin X B, Boutin J, Martin N and Spurgeon P. 2012b. Optimization of L-Band sea surface emissivity models deduced from SMOS data. IEEE Transactions on Geoscience and Remote Sensing, 50(5): 1414-1426 [DOI: 10.1109/TGRS.2012.2184547]